Aptamer Clicked Poly(ferrocenylsilanes) at Au Nanoparticles as Platforms with Multiple Function

Tibor Halmagyi, Nizar Alsharif, Mohamed Berkal, Mark Hempenius, Istvan Szilagyi, G. Julius Vancso, Corinne Nardin

RESEARCH ARTICLE

Aptamer Clicked Poly(ferrocenylsilanes) at Au Nanoparticles as Platforms with Multiple Functions

Tibor G. Halmagyi[a], Nizar B. Alsharif[c], Mohamed A. Berkal[a], Mark A. Hempenius[b], Istvan Szilagyi[c], G. Julius Vancso*[b], Corinne Nardin[a]*

[a] Tibor G. Halmagyi, Mohamed A. Berkal, Corinne Nardin
E2S UPPA, CNRS, IPREM
Universite de Pau et des Pays de l'Adour
F-64053 Pau, France
[b] Mark A. Hempenius, G. Julius Vancso
Sustainable Polymer Chemistry
University of Twente
NL-7522NB Enschede, the Netherlands
[c] Nizar B. Alsharif, Istvan Szilagyi
MTA-SZTE Momentum Biocolloids Research Group, Department of Physical Chemistry and Materials Science, Interdisciplinary Research Center
University of Szeged
H-6720 Szeged, Hungary
* Corresponding authors: Email: g.j.vancso@utwente.nl; corinne.nardin@univ-pau.fr

Supporting information for this article is given via a link at the end of the document.

Abstract: Aptamers are widely used in biosensing due to their specific sensitivity toward many targets. Thus, gold nanoparticle (AuNP) aptasensors are subject to intense research due to the complementary properties of aptamers as sensing elements and AuNPs as transducers. We present herein a novel method for the functional coupling of thrombin-specific aptamers to AuNPs via an anionic, redox-active poly(ferrocenylsilane) (PFS) polyelectroyte. The polymer acts as a co-reductant and stabilizer for the AuNPs, provides grafting sites for the aptamer, and can be used as a redox sensing element, making the aptamer-PFS-AuNP composite (aptamer-AuNP) a promising model system for future multifunctional sensors. The aptamer-AuNPs exhibit excellent colloidal stability in high ionic strength environments owing to the combined electrosteric stabilizing effects of the aptamer and the PFS. The synthesis of each assembly element is described, and the colloidal stability and redox responsiveness are studied. As an example to illustrate applications, we present results for thrombin sensitivity and specificity using the specific aptamer.

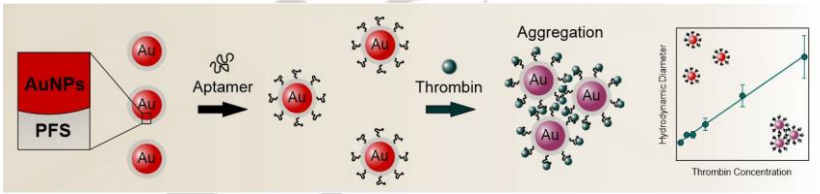

Table of Contents: We present a novel poly(ferrocenylsilane)-gold nanoparticle (PFS-AuNP) system for aptamer grafting. A multi-responsive aptamer-AuNP platform is described. This platform possesses high colloidal stability in high ionic strength environments and exhibits both a redox response and the specific sensitivity of the aptamer.

Introduction

Aptamer-based systems are an essential angle of research in the biosensing community[1,2]. Aptamers are single-stranded DNA (ssDNA) sequences of generally a few tens[3] of nucleic acid units. However, aptamers of as many as 84 units are also described[4], with a specific sensitivity towards a target molecule. Usually developed with the method known as systematic evolution of ligands by exponential enrichment (SELEX)[5], these custom-made aptamer biomolecules are used as receptors for a wide variety of targets such as proteins[6–8], pesticides[9–11], drugs[12–24], heavy metal ions[25–27], and others[28–33].

One of the most frequently employed aptamers is the thrombin-specific oligonucleotide strand. The active conformation of these aptamers is a G-quadruplex[6,34] structure made possible by the abundance of guanine bases in the oligonucleotide chain. The thrombin protein can interact with this structure, forming a solid connection via H-bonds and structural changes in the aptamer chain[6]. Due to the well-studied interaction between the aptamer and its target in this case, thrombin is helpful as a model target for testing novel aptasensor platforms.

Aptamers are particularly effective when coupled with a simple and relatively cheap transducer like gold nanoparticles (AuNPs)[11,26,35–38]. AuNPs are well-known for their size-dependent absorbance due to the localized surface plasmon resonance (LSPR) effect[39]. Several biosensors utilize such effects in systems based on target-induced aggregation of AuNPs[8,10–14,40–49]. Usually, the detection method in these biosensors uses colorimetry, following the red-blue color change upon aggregation of AuNPs, or UV-visible spectroscopy if the nanoparticle concentration is too low to detect the color change with the eye.

Biomolecules are known to stabilize metal nanoparticles in colloidal dispersions. It has been shown for both enzymes[50] and aptamers[51–55] that these macromolecules exhibit repulsive steric effects[56], making colloidal stabilization possible even at very high electrolyte concentrations, at which electrostatic effects are

screened. To fully use such electrosteric stabilization, covalent grafting of the aptamer to the AuNPs is preferred to simple adsorption[28,52]. Here, we use redox-responsive polyelectrolytes based on poly(ferrocenylsilane) (PFS) backbones[57,58]. Coupled with the capacity of anionic PFS polyelectrolytes to provide additional electrosteric stabilization to colloidal nanoparticle dispersions[59,60], aptamer-PFS-gold nanoparticle hybrids show promise as highly stable colloidal systems even at electrostatic screening conditions.

PFSs have been shown to reduce metal salts and stabilize thus-formed metal nanoparticles (MNPs) in electrolytes [59] and in hydrogel matrices[61–63]. The variety of side chains and the metals used makes these PFS-MNPs potentially useful in several fields for biological[63] and redox sensing[57,61] applications. In this article, we show the synthesis and characterization of an assembly of aptamers and PFS-AuNPs with remarkable colloidal stability and redox sensitivity owing to the PFS and thrombin sensitivity through the functional covalently surface-immobilized aptamer. Such assemblies, of which a model system for thrombin detection was created here as a proof-of-concept, would represent an improvement over more traditional gold nanoparticle aptasensors due to the high salt-stability provided by the polyelectrolyte-aptamer composite and the possibility for surface charge tuning via reduction/oxidation of the poly(ferrocenylsilane).

Results and Discussion

Synthesis of Polymers

^{1}H NMR spectra up to and including **3** (See Scheme S1, PFS-I / $N_{3(20\ \%)}$) are in line with previous literature data[58]. For the water-soluble polymer **4**, a full peak assignment is presented in the "poly(ferrocenylsilane) (PFS) synthesis" section of the Supporting Information (SI). The lack of doubled 1-CH_2 and 2-CH_2 peaks (which would indicate remaining PFS-I repeat units) provides additional proof of synthesis, which, together with the water-solubility of the polymer, indicate full conversion of the iodopropyl moieties (Figures S1-S3).

Polymer Grafting to PFS^{-}N$_{3\ (20\ \%)}$

To ascertain the applicability of the strain-promoted azide-alkyne cycloaddition, we used m-dPEG$_{12}$-DBCO oligomer in a grafting reaction with our PFS$^{-}N_{3(20\ \%)}$ polymer. The products of this reaction were investigated with ^{1}H and ^{13}C NMR (see SI, Figures S4-S7) ATR-FTIR. The results of these experiments are presented in Figure 1.

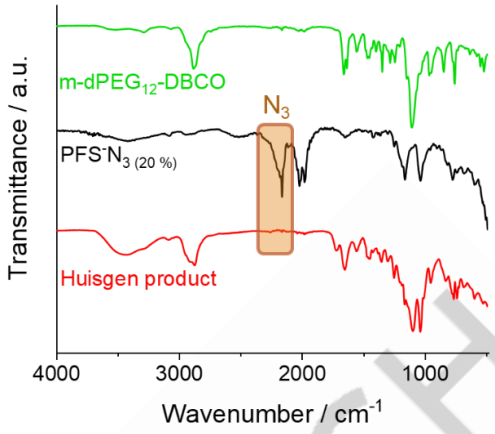

Figure 1. ATR-FTIR spectroscopy results on PFS$^{-}N_{3(20\ \%)}$ + m-dPEG$_{12}$-DBCO oligomer grafting experiments. The location of the azide band at 2200 cm^{-1}, used to determine the success of the grafting, is highlighted in orange on the relevant spectra.

As Figure 1 shows, the characteristic band of the azide moiety at 2200 cm^{-1} is clearly present in the original polymer, but after reaction with m-dPEG$_{12}$-DBCO either in water or in DMSO, it disappears. This points to successful grafting, a result also confirmed by ^{1}H and ^{13}C NMR (See SI Figures S4-S7). As seen on the ^{1}H NMR spectrum of the reaction product (Figure S6), the polymer and the m-dPEG12-DBCO peaks are present. Still, significant changes (widening of peaks, the appearance of new ones at 7.90 and 6.65 ppm) can be observed in the DBCO aromatic region (6.5-8 ppm). Additionally, the blue highlighted area of the ^{13}C NMR comparison in Figure S7 indicates changes in the aromatic region of the m-dPEG$_{12}$-DBCO, as the azide-alkyne cycloaddition induces changes in the chemical environments of the benzene rings (carbon atoms marked with "a" on Scheme S2). Peaks of the newly formed 1,2,3-triazole ring also appear in this region.

Aptamer Grafting to PFS^{-}N$_{3\ (20\ \%)}$, Enzymatic Digestion

Grafting of the aptamer to PFS$^{-}N_{3\ (20\ \%)}$ followed a similar principle as the experiments with the m-dPEG$_{12}$-DBCO oligomer. However, a separate characterization method was required due to the lower synthesis scale.

Exonucleases with 5' → 3' (RecJf) and 3' → 5' (Exonuclease I) digestion activity were used to test the Huisgen grafting of the aptamer to PFS or PFS-AuNP. The premise of this experiment was that both the RecJf and the Exonuclease I enzyme could fully digest aptamer strands that are not attached to the polymer (Scheme 1. a). Still, after the grafting, the 5' end of the aptamer becomes inaccessible to the RecJf enzyme, thereby hindering digestion. In contrast, the 3' → 5' digestion activity of the Exonuclease I enzyme remains unaffected (Scheme 1. b). Using a fluorescent dye such as SYBR Gold makes undigested ssDNA strands visible in fluorescence spectroscopy measurements (Scheme 1. c). The single nucleotides or very short oligomers that remain after successful enzymatic degradation, however, do

not intercalate with SYBR Gold; thus, fluorescence is not observed (Scheme 1. d).

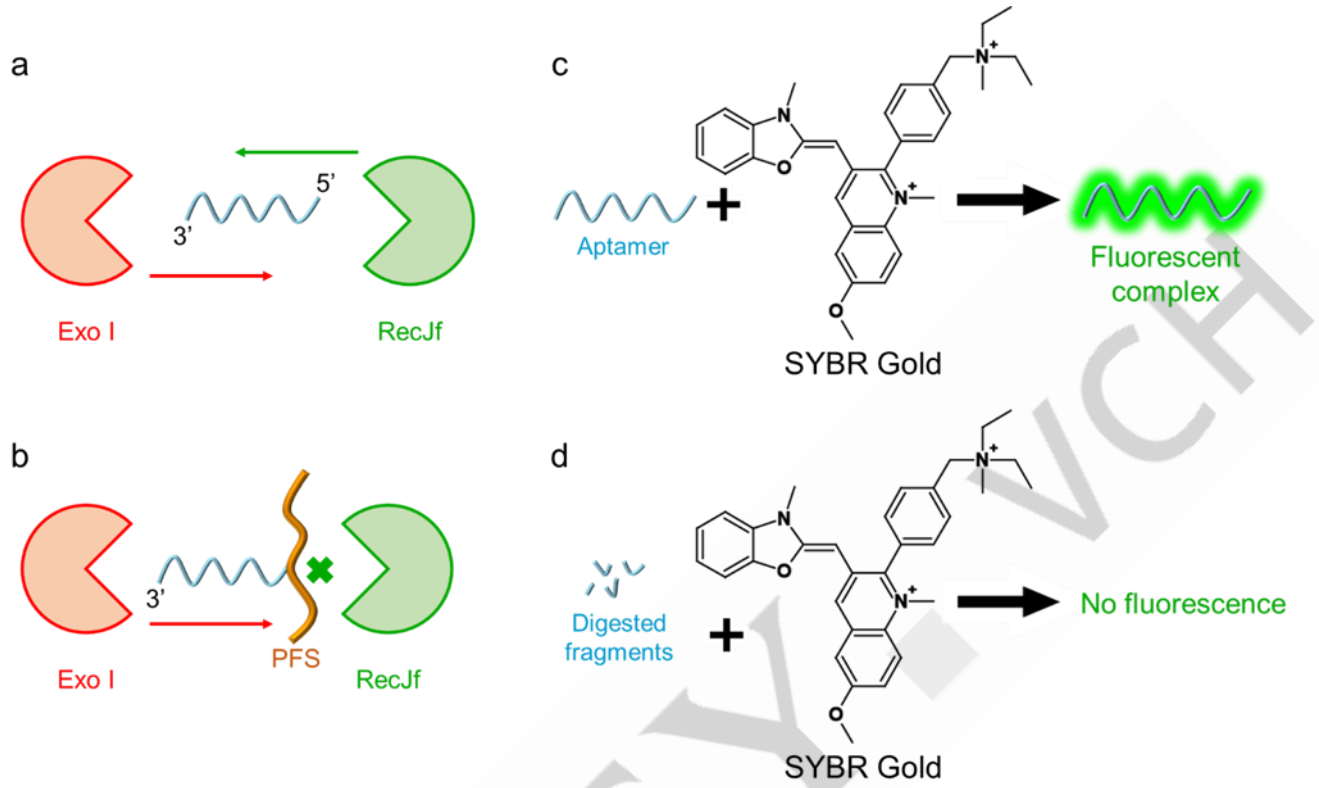

Scheme 1. Illustration of the dual enzymatic digestion method used to confirm the grafting of the aptamer to PFS and PFS / AuNP samples. Enzymatic digestion of the free aptamer (a). Enzymatic digestion of aptamer-PFS hybrid, hindered at the 5' end (b). Aptamers form fluorescent complexes with the SYBR Gold dye (c). Digested fragments do not form fluorescent complexes with the SYBR Gold fluorescent dye (d).

Testing of this principle yielded the data captured in Figure 2. Both the aptamer and the aptamer-PFS samples exhibit high fluorescence, which disappears in both cases upon the addition of the Exonuclease I enzyme. However, the fluorescence only decreases upon the addition of RecJf to the aptamer sample and remains high upon the enzyme's addition to the PFS-grafted aptamer. This points to successful grafting, as the loss of the RecJf's activity indicates the Huisgen-reaction-induced inaccessibility of the 5' end of the aptamer.

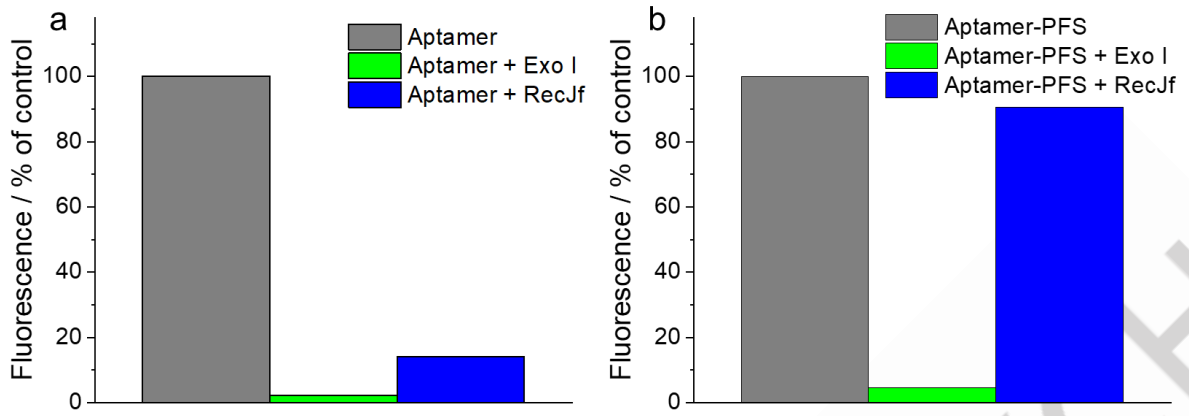

Figure 2. Results of the fluorescence measurements of aptamer samples after dual enzymatic digestion without PFS (a) and with it (b).

Aptamer Grafting to PFS-AuNPs

The process of both the grafting of the aptamer to the PFS-coated AuNPs and the testing of the grafting is akin to the procedures described above in the aptamer grafting to the PFS-$N_{3\,(20\,\%)}$ section. The results obtained from these experiments are shown in Figure 3.

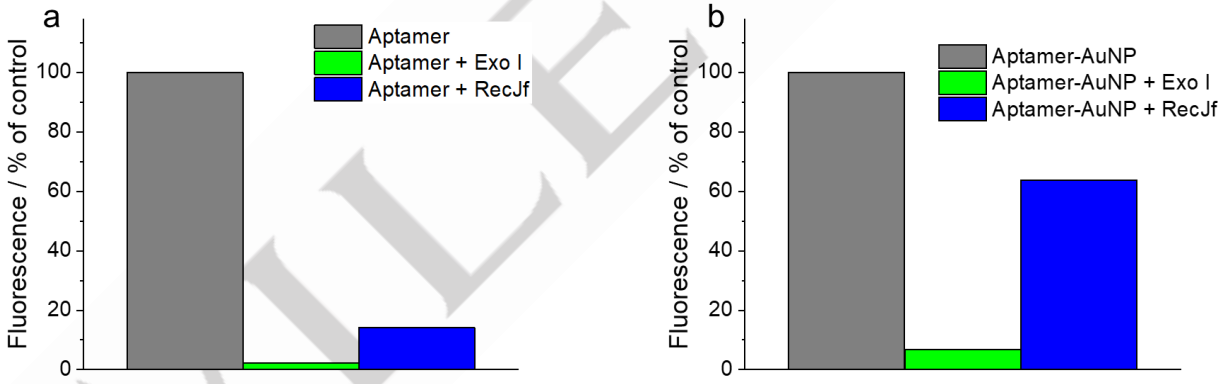

Figure 3. Fluorescence spectroscopy results after dual enzymatic digestion without PFS-AuNPs (a) and with (b).

As previously observed, the high fluorescence exhibited by the enzyme-free samples disappears upon the addition of Exonuclease I. When the aptamer is either grafted to polymers or AuNPs, hindered digestion in the case of RecJf is observed, indicating successful grafting. This finding was corroborated by the electrophoretic light scattering (ELS) results, which show that the electrophoretic mobility of the gold nanoparticles increases slightly upon the addition of the aptamer (from (-0.22 ± 0.06) µm cm V^{-1} s^{-1} to (-0.30 ± 0.14) µm cm V^{-1} s^{-1}). It must be noted that UV-visible spectra of the AuNPs and the aptamer-AuNPs overlap, as shown in Figure S8.

Colloidal Stability of AuNPs

The colloidal stability of the gold nanoparticles was assessed by preparing nanoparticle suspensions of different concentrations in 1 M NaCl (Figure 4. A and Figure S9) and then determining the Stokes effective hydrodynamic diameter vs. time values. Colloidal stability was also assessed in the aptamer interaction buffer (Figure S10). The particle concentrations ranged from 0.2 ppm (1.0 µM Au) to 10 ppm (50.6 µM Au).

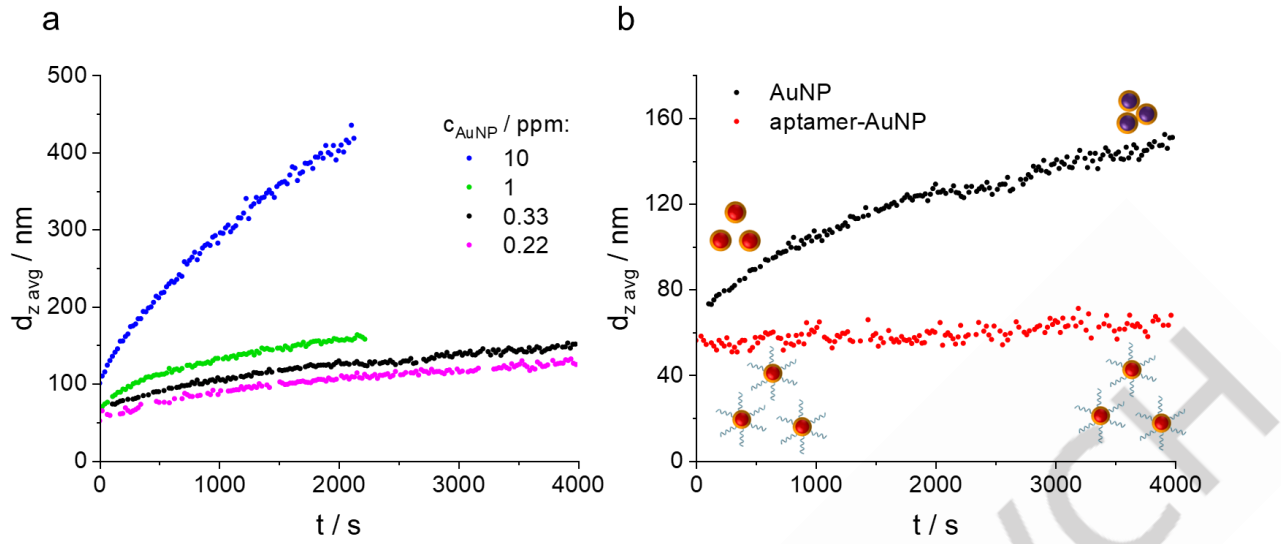

Figure 4. DLS data showing the Stokes effective hydrodynamic diameter values vs. time of PFS-AuNPs in 1 M NaCl (a). Comparison of stability of 0.33 ppm aptamer-AuNPs & PFS-AuNPs in 1 M NaCl (b).

Note that under these experimental conditions, the dissolved ions screen the electrostatic repulsion, and the particles undergo rapid aggregation due to dispersion forces in case of the absence of repulsion of non-electrostatic origin, such as steric interaction[64]. It is evident from the data that in concentrations up to at least 1 ppm, diffusion-limited aggregation is significantly slower, with only a twofold increase in diameter over 2000 s in a high ionic-strength dispersion (Figure 4. a). This observation is in line with previous results for PFS-stabilized nanoparticles[59,60]. Literature data indicate that aptamer grafting would further improve this stability via steric effects[54,55]. To test this possibility, we compared the stability of aptamer-grafted AuNPs to that of AuNPs without aptamer (Figure 4. b). The concentration for these measurements was chosen to be 0.33 ppm (1.67 µM Au, 1 µM aptamer), the same as in the thrombin sensing experiments. The aptamer-AuNPs are exceedingly stable at this concentration, while DLS still shows a good signal-to-noise ratio.

The stability of the nanoparticles was greatly enhanced by modifying the AuNP surface with aptamers. After 4000 s, a 5 times lower size increase was observed in the presence of aptamer than without it. This is explained by the fact that the grafted aptamers point outwards from the AuNP core, forming a steric barrier around the particles.

Redox Activity of the PFS and its Effects on Colloidal Stability

To probe the redox activity of PFS, we tested the impact of 50 µM $FeCl_3$ on 10 µM PFS-AuNP and 10 µM aptamer-AuNP. As shown in Figure 5, the expected aggregation occurred in both cases, but the size of the aptamer-AuNP aggregates (Figure 5. b) was an order of magnitude higher than that of the PFS-AuNPs (Figure 5. a). This is probably due to the bridging effect of the ssDNA strands. After adding 100 µM vitamin C to the particles, no reduction-driven disaggregation was observed, with the perceived size decrease in the case of the aptamer-AuNPs due to sedimentation (Figure S11). These results indicate that the redox activity of the particles is unaffected by the aptamer grafting, rendering the aptamer-AuNPs dual-responsive and opening the door to improving the detection limit by tuning the oxidation state of PFS.

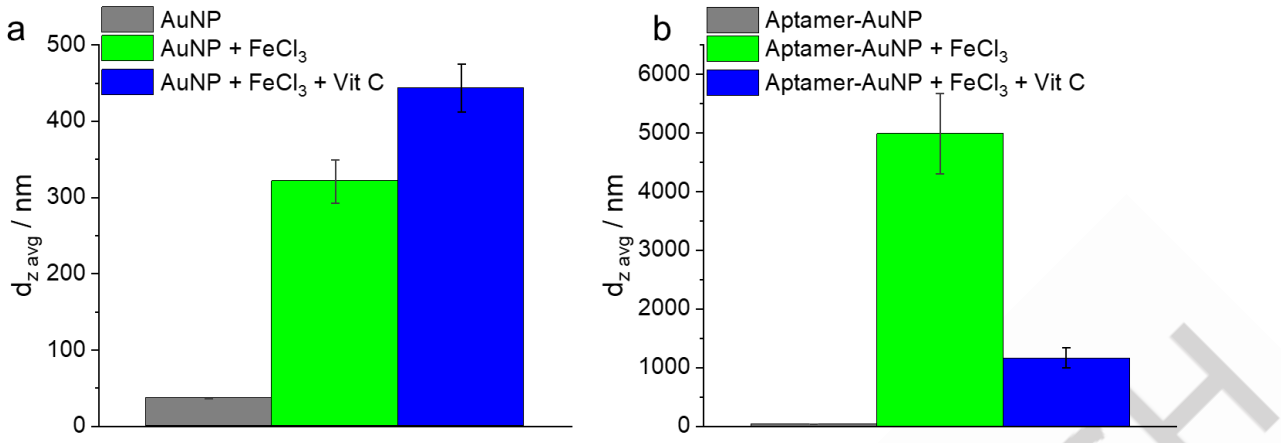

Figure 5. Results of redox activity tests on PFS-AuNPs (a) and aptamer-AuNPs (b). Gold concentration was 10 µM in each measurement. In the redox tests, 50 µM $FeCl_3$ and 100 µM ascorbic acid were used.

UV-visible measurements (Figure 6) confirm the oxidation-based aggregation of both AuNPs and aptamer-AuNPs, a DLS-based indication for which was previously shown in Figure 5. The plasmonic peak of AuNPs at 540 nm – characteristic of AuNPs of sub-50 nm diameter, as shown by transmission electron microscopy (TEM) imaging (see Figure S12) – disappears for AuNPs (Figure 6. a) as well as for aptamer-AuNPs (Figure 6. b).

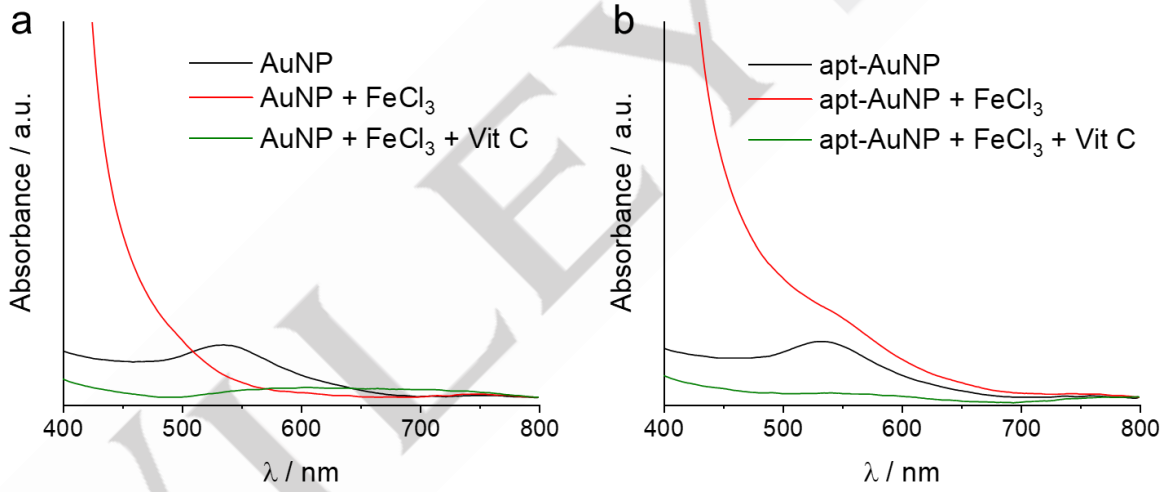

Figure 6. UV-visible spectra of redox tests with AuNPs (a) and aptamer-AuNPs (b).

The stability of the aptamer-AuNPs was also determined against thrombin. Proteins are notorious for adhering to surfaces, and thrombin, in particular, shows affinity toward polar surfaces[65]. Thus, investigations of the interaction between thrombin and the AuNPs were necessary. In these experiments, the structuring of the aptamer was not performed to avoid aptamer-thrombin interaction. Results are shown in Figure 7.

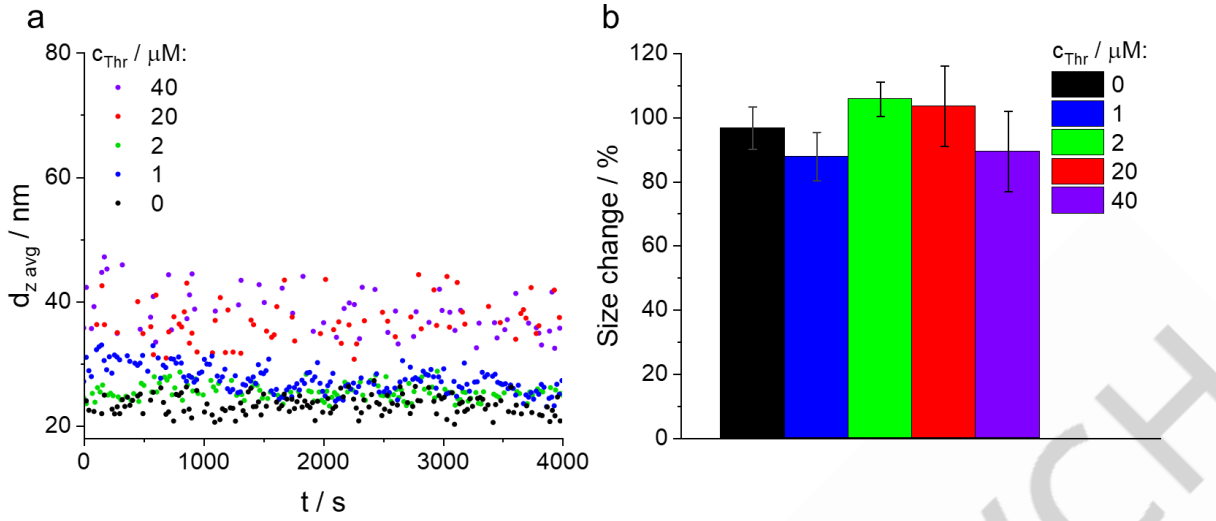

Figure 7. Stability tests (values of the Stokes effective hydrodynamic diameter) over time of aptamer-AuNPs as measured by DLS in 1 x interaction buffer (a). The ratio of mean nanoparticle diameter at the end and the beginning of the measurement (b) (gold concentration was 0.33 ppm in all samples).

The aptamer-AuNPs were stable in up to 40 µM thrombin (Figure 7. a), as no significant size change was observed over 4000 s (Figure 7. b). As this is far beyond the concentrations necessary for the sensing measurements, the stability of the nanoparticles vs. thrombin dose was determined to be suitable for our purposes.

Thrombin Sensing and Selectivity

The interaction of the aptamer-AuNPs with thrombin is illustrated in Scheme 2. In the first step, the aptamers are straightened by annealing to provide maximum steric stabilization to the polymer and ensure the correct conformation for specific interaction with the target[4]. Then, the addition of the interaction buffer induces the formation of the active G-quadruplex aptamer conformation. In the last step, thrombin is introduced, destabilizing the colloidal dispersion by hindering the steric stabilization effect of the aptamers. At high enough electrolyte concentrations, this results in the aggregation of the aptamer-AuNPs, which can be followed by DLS, UV-visible spectroscopy, or the naked eye, depending on the aptamer-AuNP concentration. This interaction, and thus the collapse of the colloidal stability of the AuNPs, is specific to thrombin and cannot be induced by other proteins.

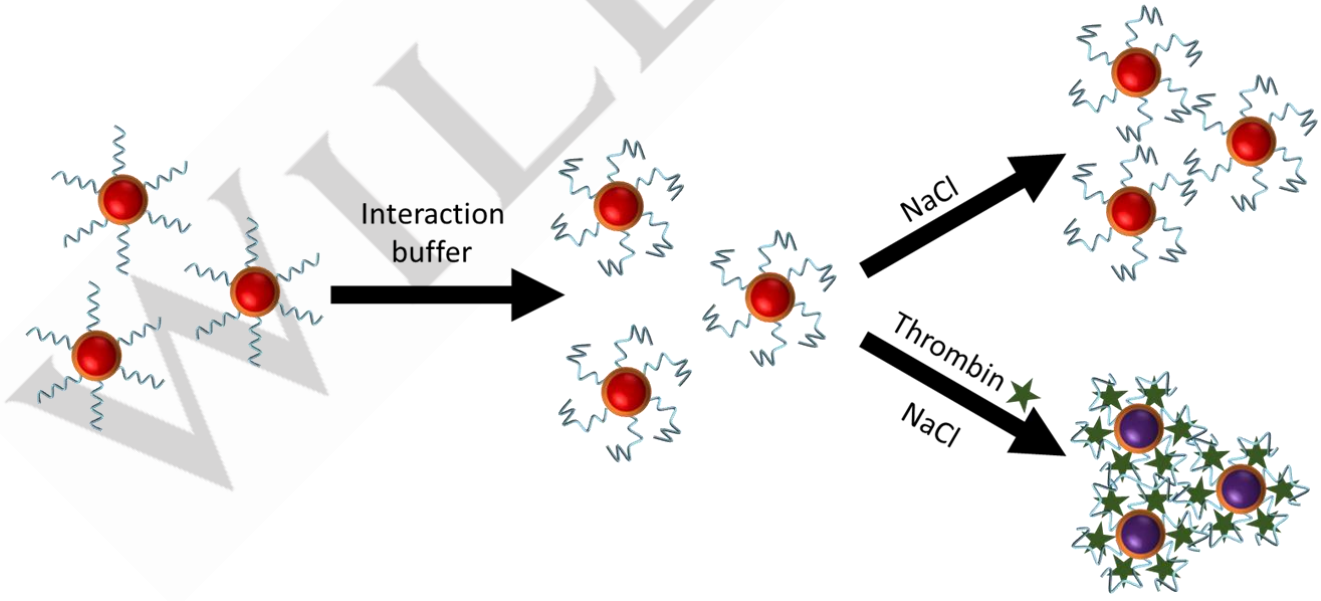

Scheme 2. Schematic representation of the working principle of the thrombin-specific aptamer-AuNP model nanosensor.

Thrombin sensing experiments were monitored by DLS by measuring the Stokes effective hydrodynamic diameter via the protocol outlined in the materials and methods section of the Supporting Information. After structuring the aptamer in the interaction buffer and thrombin-aptamer interaction, 1 M NaCl was added to the solution, and the mixture was left to stand for an hour. Figure 8 shows DLS measurement results after this aggregation time.

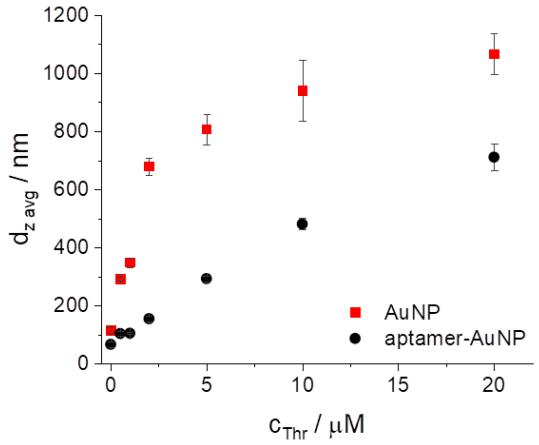

Figure 8. DLS results (hydrodynamic diameter) versus thrombin concentration in 1x buffer and 1 M NaCl (gold concentration was 0.33 ppm in all samples).

As shown, both the AuNP and the aptamer-AuNP aggregate upon the addition of thrombin. For both systems, a LOD ≤ 0.5 µM was found. The AuNP response was not linear, but for the aptamer-AuNP, a linear range between 0 – 10 µM was found.
To demonstrate that the aptamer remains functional after grafting, proof of selectivity was required. To this end, we repeated the above experiment with beta-lactoglobulin instead of thrombin. This protein does not interact with the thrombin-specific aptamer; thus, it can be used as a target protein in a control experiment. The same 0.5 µM – 20 µM protein concentration was used for the thrombin sensing tests presented above. The results are shown in Figure 9.

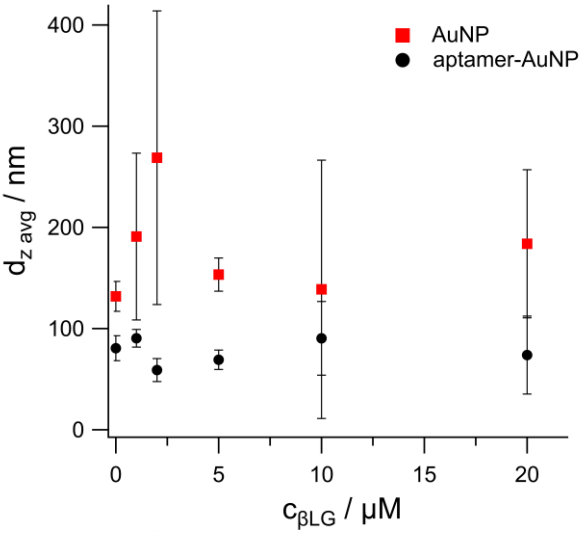

Figure 9. DLS results of the beta-lactoglobulin response of the gold nanoparticle and the aptamer-AuNPs in the presence of 1 x buffer and 1 M NaCl (gold concentration was 0.33 ppm in all samples).

The non-aptamer-grafted AuNPs show significantly increased diameters in 1 M NaCl if beta-lactoglobulin is present in the system. However, as the large error bars indicate, the samples were very polydisperse, containing aggregates. Interestingly, the beta-lactoglobulin produces smaller AuNP aggregates than thrombin (ca. 200 nm vs ca. 1000 nm). This might be due to beta-lactoglobulin's much lower molecular weight (18.4 kDa vs 33.6 kDa for thrombin).
In contrast, the colloidal stability of the aptamer-AuNPs is seemingly unaffected by any concentration of beta-lactoglobulin. This is probably because the aptamers continue providing steric stabilization to the nanoparticles, as they do not interact with this protein. This shows that the aptamer-AuNP system is functional.

Conclusion

In summary, a novel way of functional grafting of aptamers to gold nanoparticles exhibiting multiple activities (steric stabilization, redox sensitivity, and specific sensitivity to the aptamer target) is described. Water soluble anionic poly(ferrocenylsilane), whose synthesis is also described in detail, plays the role of co-reductant and stabilizer in the AuNP synthesis as well as the grafting site of the aptamer via strain-promoted azide-alkyne cycloaddition. This grafting was thoroughly tested and characterized by multiple methods. The complete platform shows outstanding colloidal stability owing to the steric stabilization of the aptamer ssDNA strands. The redox activity of the PFS remains after grafting and provides further possibilities for increasing the sensitivity of a future sensor based on this method. The thrombin aptamer remains functional after grafting, and the gold nanoparticles make detecting the aptamer-target interaction possible. One further novelty is the colloidal approach to characterizing nanoparticle aggregation via DLS, which gives size data directly in dispersions, unlike electron microscopy and similar techniques.

Supporting Information

The supporting information containing materials and experimental methods, NMR spectra, buffer stability measurement data, and photographs is available online. Additional references have been cited in the supporting information[66–68].

Conflicts of Interest

The authors declare no conflicts of interest.

Acknowledgements

The authors (CN) acknowledge grants from the French National Centre for Scientific Research (International Emerging Action ASIDE), the Universite de Pau et de Pays de l'Adour through its project Energy and Environment Solutions supported by the Agence National pour la recherche (ANR OPE-2018-0020). I.S. is grateful to the Hungarian Academy of Sciences for funding through the Momentum project LP2022-16/2022. The authors

gratefully acknowledge the help of Voichita Mihali of the University of Basel for her help with the transmission electron microscopy imaging.

Keywords: Aptamer, gold nanoparticle, aptasensor, redox polyelectrolyte, colloidal stability

References

[1] L. Hosseinzadeh, M. Mazloum-Ardakani, *Adv Clin Chem* **2020**, *99*, 237–279.
[2] X. Kou, X. Zhang, X. Shao, C. Jiang, L. Ning, *Analytical and Bioanalytical Chemistry 2020 412:25* **2020**, *412*, 6691–6705.
[3] H. Hasegawa, N. Savory, K. Abe, K. Ikebukuro, A. O. A. Miller, J. Jacques, V. Eynde, *Molecules 2016, Vol. 21, Page 421* **2016**, *21*, 421.
[4] M. A. Berkal, Q. Palas, E. Ricard, C. Lartigau-Dagron, L. Ronga, J.-J. Toulmé, C. Parat, C. Nardin, *Macromol Biosci* **2023**, 2200508.
[5] S. C. B. Gopinath, *Anal Bioanal Chem* **2007**, *387*, 171–182.
[6] B. Deng, Y. Lin, C. Wang, F. Li, Z. Wang, H. Zhang, X. F. Li, X. C. Le, *Anal Chim Acta* **2014**, *837*, 1–15.
[7] A. Bini, M. Minunni, S. Tombelli, S. Centi, M. Mascini, *Anal Chem* **2007**, *79*, 3016–3019.
[8] Y. Jiang, M. Shi, Y. Liu, S. Wan, C. Cui, L. Zhang, W. Tan, *Angewandte Chemie - International Edition* **2017**, *56*, 11916–11920.
[9] R. Bala, S. Dhingra, M. Kumar, K. Bansal, S. Mittal, R. K. Sharma, N. Wangoo, *Chemical Engineering Journal* **2017**, *311*, 111–116.
[10] R. Bala, R. K. Sharma, N. Wangoo, *Anal Bioanal Chem* **2016**, *408*, 333–338.
[11] W. Bai, C. Zhu, J. Liu, M. Yan, S. Yang, A. Chen, *Environ Toxicol Chem* **2015**, *34*, 2244–2249.
[12] J. Ping, Z. He, J. Liu, X. Xie, *Electrophoresis* **2018**, *39*, 486–495.
[13] K. M. Song, M. Cho, H. Jo, K. Min, S. H. Jeon, T. Kim, M. S. Han, J. K. Ku, C. Ban, *Anal Biochem* **2011**, *415*, 175–181.
[14] Q. Ma, Y. Wang, J. Jia, Y. Xiang, *Food Chem* **2018**, *249*, 98–103.
[15] A. Chen, X. Jiang, W. Zhang, G. Chen, Y. Zhao, T. M. Tunio, J. Liu, Z. Lv, C. Li, S. Yang, *Biosens Bioelectron* **2013**, *42*, 419–425.
[16] Z. Yan, N. Gan, D. Wang, Y. Cao, M. Chen, T. Li, Y. Chen, *Biosens Bioelectron* **2015**, *74*, 718–724.
[17] K. Abnous, N. M. Danesh, M. Ramezani, A. S. Emrani, S. M. Taghdisi, *Biosens Bioelectron* **2016**, *78*, 80–86.
[18] Y. S. Kim, J. H. Kim, I. A. Kim, S. J. Lee, J. Jurng, M. B. Gu, *Biosens Bioelectron* **2010**, *26*, 1644–1649.
[19] M. Ramezani, N. Mohammad Danesh, P. Lavaee, K. Abnous, S. Mohammad Taghdisi, *Biosens Bioelectron* **2015**, *70*, 181–187.
[20] Y. Luo, J. Xu, Y. Li, H. Gao, J. Guo, F. Shen, C. Sun, *Food Control* **2015**, *54*, 7–15.
[21] N. Zhou, J. Wang, J. Zhang, C. Li, Y. Tian, J. Wang, *Talanta* **2013**, *108*, 109–116.
[22] A. S. Emrani, N. M. Danesh, P. Lavaee, M. Ramezani, K. Abnous, S. M. Taghdisi, *Food Chem* **2016**, *190*, 115–121.
[23] N. M. Danesh, M. Ramezani, A. S. Emrani, K. Abnous, S. M. Taghdisi, *Biosens Bioelectron* **2016**, *75*, 123–128.
[24] K. M. Song, E. Jeong, W. Jeon, M. Cho, C. Ban, *Anal Bioanal Chem* **2012**, *402*, 2153–2161.
[25] Y. Wang, F. Yang, X. Yang, *Biosens Bioelectron* **2010**, *25*, 1994–1998.
[26] L. Li, B. Li, Y. Qi, Y. Jin, *Anal Bioanal Chem* **2009**, *393*, 2051–2057.
[27] Y. Wu, L. Liu, S. Zhan, F. Wang, P. Zhou, *Analyst* **2012**, *137*, 4171–4178.
[28] R. Cheng, S. Liu, H. Shi, G. Zhao, *J Hazard Mater* **2018**, *341*, 373–380.
[29] F. Li, J. Zhang, X. Cao, L. Wang, D. Li, S. Song, B. Ye, C. Fan, *Analyst* **2009**, *134*, 1355–1360.
[30] Y. Mao, T. Fan, R. Gysbers, Y. Tan, F. Liu, S. Lin, Y. Jiang, *Talanta* **2017**, *168*, 279–285.
[31] M. Jo, J. Y. Ahn, J. Lee, S. Lee, S. W. Hong, J. W. Yoo, J. Kang, P. Dua, D. K. Lee, S. Hong, S. Kim, *Oligonucleotides* **2011**, *21*, 85–91.
[32] E. H. Lee, S. K. Lee, M. J. Kim, S. W. Lee, *Food Chem* **2019**, *287*, 205–213.
[33] J. Feng, Q. Shen, J. Wu, Z. Dai, Y. Wang, *Food Control* **2019**, *98*, 333–341.
[34] L. Zhang, X. Zhang, P. Feng, Q. Han, W. Liu, Y. Lu, C. Song, F. Li, *Anal Chem* **2020**, *92*, 7419–7424.
[35] V. X. T. Zhao, T. I. Wong, X. T. Zheng, Y. N. Tan, X. Zhou, *Mater Sci Energy Technol* **2020**, *3*, 237–249.
[36] B. Liu, J. Zhuang, G. Wei, *Environ Sci Nano* **2020**, *7*, 2195–2213.
[37] Y. Zheng, Y. Wang, X. Yang, *Sens Actuators B Chem* **2011**, *156*, 95–99.
[38] C. C. Chang, C. P. Chen, T. H. Wu, C. H. Yang, C. W. Lin, C. Y. Chen, *Nanomaterials* **2019**, *9*, 1–24.
[39] K. M. Mayer, J. H. Hafner, *Chem Rev* **2011**, *111*, 3828–3857.
[40] Z. Chen, Y. Huang, X. Li, T. Zhou, H. Ma, H. Qiang, Y. Liu, *Anal Chim Acta* **2013**, *787*, 189–192.
[41] C. Yang, Y. Wang, J. L. Marty, X. Yang, *Biosens Bioelectron* **2011**, *26*, 2724–2727.
[42] X. Ma, L. Song, N. Zhou, Y. Xia, Z. Wang, *Int J Food Microbiol* **2017**, *245*, 1–5.
[43] J. Liu, Y. Lu, *Nat Protoc* **2006**, *1*, 246–252.
[44] H. Wei, B. Li, J. Li, E. Wang, S. Dong, *Chemical Communications* **2007**, 3735–3737.
[45] J. Liu, Z. Guan, Z. Lv, X. Jiang, S. Yang, A. Chen, *Biosens Bioelectron* **2014**, *52*, 265–270.
[46] C. C. Huang, Y. F. Huang, Z. Cao, W. Tan, H. T. Chang, *Anal Chem* **2005**, *77*, 5735–5741.
[47] Y. Xie, Y. Huang, D. Tang, H. Cui, L. Yang, H. Cao, W. Yun, *New Journal of Chemistry* **2019**, *43*, 4531–4538.
[48] Y. S. Borghei, M. Hosseini, M. Dadmehr, S. Hosseinkhani, M. R. Ganjali, R. Sheikhnejad, *Anal Chim Acta* **2016**, *904*, 92–97.
[49] X. Li, R. Cheng, H. Shi, B. Tang, H. Xiao, G. Zhao, *J Hazard Mater* **2016**, *304*, 474–480.
[50] R. Savin, C. Blanck, N. O. Benzaamia, F. Boulmedais, *Molecules* **2022**, *27*, 3309.
[51] P. A. Mirau, J. E. Smith, J. L. Chávez, J. A. Hagen, N. Kelley-Loughnane, R. Naik, *Langmuir* **2018**, *34*, 2139–2146.
[52] C. Sun, S. Zhao, F. Qu, W. Han, J. You, *Microchimica Acta* **2020**, *187*, 1–9.
[53] Z. Xiao, O. C. Farokhzad, *ACS Nano* **2012**, *6*, 3670–3676.
[54] W. Zhao, M. A. Brook, Y. Li, *ChemBioChem* **2008**, *9*, 2363–2371.
[55] W. Zhao, W. Chiuman, M. A. Brook, Y. Li, *ChemBioChem* **2007**, *8*, 727–731.
[56] S. R. Raghavan, G. Fritz, E. W. Kaler, *Langmuir* **2002**, *18*, 3797–3803.
[57] J. Song, Y. N. Tan, D. Jańczewski, M. A. Hempenius, J. W. Xu, H. R. Tan, G. J. Vancso, D. Janczewski, M. A. Hempenius, J. W. Xu, H. R. Tan, G. J. Vancso, D.

Jańczewski, M. A. Hempenius, J. W. Xu, H. R. Tan, G. J. Vancso, *Nanoscale* **2017**, *9*, 19255–19262.
[58] M. A. Hempenius, F. F. Brito, G. J. Vancso, *Macromolecules* **2003**, *36*, 6683–6688.
[59] J. Song, Y. N. Tan, D. Jańczewski, M. A. Hempenius, J. W. Xu, H. R. Tan, G. J. Vancso, *Nanoscale* **2017**, *9*, 19255–19262.
[60] N. B. Alsharif, T. G. Halmágyi, M. A. Hempenius, G. J. Vancso, C. Nardin, I. Szilagyi, *Nanoscale* **2023**, DOI 10.1039/D3NR02063K.
[61] X. Feng, M. A. Hempenius, G. J. Vancso, *Macromol Chem Phys* **2018**, *219*, 1800223.
[62] T. Halmagyi, J. Hao, M. A. Hempenius, G. J. Vancso, *ACS Appl Nano Mater* **2022**, *5*, 8868–8874.
[63] X. Sui, X. Feng, A. Di Luca, C. A. Van Blitterswijk, L. Moroni, M. A. Hempenius, G. J. Vancso, *Polym Chem* **2012**, *4*, 337–342.
[64] H. Holthoff, S. U. Egelhaaf, M. Borkovec, P. Schurtenberger, H. Sticher, *Langmuir* **1996**, *12*, 5541–5549.
[65] S. Alibeik, S. Zhu, J. L. Brash, *Colloids Surf B Biointerfaces* **2010**, *81*, 389–396.
[66] M. Mir, A. T. A. Jenkins, I. Katakis, *Electrochem commun* **2008**, *10*, 1533–1536.
[67] K. Zhang, M. Zhang, X. Feng, M. A. Hempenius, G. J. Vancso, *Adv Funct Mater* **2017**, *27*, 1–8.
[68] O. Alkhamis, W. Yang, R. Farhana, H. Yu, Y. Xiao, *Nucleic Acids Res* **2020**, *48*, e120–e120.